What does water in quartz tell us about volcanic processes?

Ayomide Ajayi

Advisors: Megan Newcombe and Silvia Castilla
11/28/2022

Senior Thesis Report
GEOL 394

Department of Geology
University of Maryland
College Park

Abstract

The controls on volcanic eruptive style are not well understood, but we do know that water plays an important role. The amount of water in magma controls the viscosity of the magma as well as the depth at which vapor bubbles are formed. However, water content is not the only thing controlling magma decompression as it has been observed that relatively dry magma can erupt explosively. Another important factor is the magma decompression rate, which controls the time available to form bubbles and crystals as well as the time available for vapor to escape the system as rapid decompression leads to more explosive eruptions. Two quartz phenocrysts M.C (quartz phenocryst gotten from the middle layer of the Cerro Machin Volcano's 3600yr eruption deposition and assigned the alphabet C) and M.P (quartz phenocryst gotten from the middle layer of the Cerro Machin Volcano's 3600yr eruption deposition and assigned the alphabet P) were analyzed using FTIR. The calculated mean water concentrations of the individual points selected at the edge and center of M.C quartz are ~62.2ppm and 51.83ppm, respectively, across an average thickness of 0.0459cm while the calculated mean water concentrations of the individual points selected at the edge and center of M.P quartz are ~85.79ppm and 83.74ppm, respectively, across an average thickness of 0.0327cm. In this study, a modified Beer Lambert rule retrieved from Hencz et al. (2021) was used for diffusion modelling to constrain the magma decompression rate as well as the duration of the magma ascent. The calculations done suggest that the magma originated from a depth of ~17 km with an ascent time of ~1.25 minutes. Given that the magma storage has a minimum pressure of ~100 MPa and a maximum pressure of ~500 Mpa, the decompression rate was calculated to be between ~1.33 MPa/s and ~6.67 MPa/s. The speed at which the magma was travelling was also calculated for both the minimum and maximum pressure and estimated to be about 47.7 m/s for the minimum pressure and 238.7 m/s for the maximum pressure.

1. Introduction

Volcanic eruptions are inherently dangerous. Explosive eruptions produce hot pyroclastic flows and widespread ash deposits, which can ruin plants and crops and sometimes result in the deaths of people and animals. Explosive eruptions (**fig.1a**) also produce plumes that can rise high into the atmosphere as a result of air entrainment, which lowers the density of the plumes and increases their buoyancy. The ash from these plumes has been known to cause aircraft engine failure, and flights are often grounded in response to explosive volcanic eruptions, leading to travel disruption and economic loss. The largest volcanic eruptions can also cause changes in global climate. Effusive eruptions (**fig. 1b**) are usually less hazardous, but their associated lava flows can still destroy property and crops.

In light of the significant and varied hazards posed by volcanic eruptions, volcanologists scientists are strongly motivated to understand the controls on eruption onset and eruption style (i.e., explosive vs. effusive). The controls on volcanic eruptive style are not well understood, but we do know that water plays an important role. As magma decompresses during its journey up the volcanic conduit to the surface, water exsolves from the magma to form vapor bubbles (analogous to the formation of carbon dioxide bubbles in a bottle of coke in response to pressure release when the cap of the bottle is removed). These bubbles make the magma buoyant, and they provide the force required to accelerate the magma upwards through the crust. Knowing the original water content in the magma helps to determine the volcanic processes in the lower levels of the volcano before eruption occurred as the magma moved up the conduit.

However, the water content in a magma is not the only factor controlling eruptive style as it has been observed that relatively dry magma can erupt explosively. Another important factor that affects the eruptive style is the magma decompression rate, which controls the time available to form bubbles and crystals as well as the time available for vapor to escape the system (Cassidy et al. 2018). The eruptive style of a volcano is thought to depend on the magma decompression rate, but few constraints of magma decompression rate exist. The purpose of this study is to map water concentration in quartz to test whether water gradients in quartz if they exist could be used to put a constraint on the amount of time it took for the magma to move from the magma chamber to the surface.

Fig.1a Example of an effusive volcanic eruption. Soufriere Hills Volcano, Montserrat(Dec.1996) British Geological Survey (2022)

Fig.1b Example of an explosive volcanic eruption Soufriere Hills Volcano, Montserrat(Dec.1997) British Geological Survey (2022)

2. Geological Background

Cerro Machin Volcano is situated in the central cordillera of Colombia, South America (latitude 4.487N, longitude 75.389W), which is related to the subduction of the Nazca plate underneath the south American plate. Cerro Machin is a Quaternary dacitic volcano with an altitude of about 2750m and it has a 2.4 km wide caldera which contains three forested dacitic lava domes (Rueda et al., 2005). The volcano has had six major eruptions within the last 10,000 years and these eruptive events are known as the Espartillal (5000 yr.), P0 (4600 yr.), P1 (3600 yr.), Guaico (2600 yr.), P2 (1200 yr.), and Anillo (900 yr.) (Rueda et al., 2005). For this study, water concentration gradients will be measured in quartz crystals from the P1 eruption, which is the largest known eruption of Cerro Machin.

Hypothesis: Water concentration across quartz grains varies from center to edge.
Null hypothesis: Water concentration across the quartz phenocryst does not vary from the center to the edge (i.e., the water concentration is homogenous within the error of the measurements).

Fig. 2 Aerial view of Cerro Machin volcano (16 November 2011). Picture retrieved from the Smithsonian Institution Global Volcanism Program database. Courtesy of INGEOMINAS.

3. Literature review: Prior measurements of water in quartz phenocrysts

Measurements of water in quartz phenocrysts have been reported in just two prior studies: Tollan et al. (2019) and Jollands et al. (2020). Tollan et al. (2019) measured unexposed melt inclusions to assess the magmatic volatile equilibria of the Mesa Falls Tuff, Yellowstone, and the Jollands et al. (2020) applied experimental constraints on H-Li and H-Na diffusion in quartz to a natural quartz phenocryst from the Bishop Tuff. The authors measured water in quartz retrieved from eruptions of super volcanoes, i.e., different volcanic systems compared to the Cerro Machin Volcano; however, their methods and results provide important constraints and context for my research. Jollands et al. (2020) observe a concave-down water concentration gradient in a quartz phenocryst from the Bishop Tuff. The author relates this to the association of H with trace elements wherein the immobile (Al^{3+}) substitutes Si^{4+} and is charge-balanced either by mobile ions of Li^+ or H^+ in the quartz structure. Given that Li^+ diffuses fast, the presence of a Li^+ peak in the FTIR absorbance spectrum provides evidence that H^+ and Li^+ may have been coupled in the Bishop Tuff quartz crystal (**fig. 3**). Given the figure illustrated below, without the association of trace elements (immobile and mobile), the gradient to be expected for my research should resemble the H^+ diffusion gradient profile.

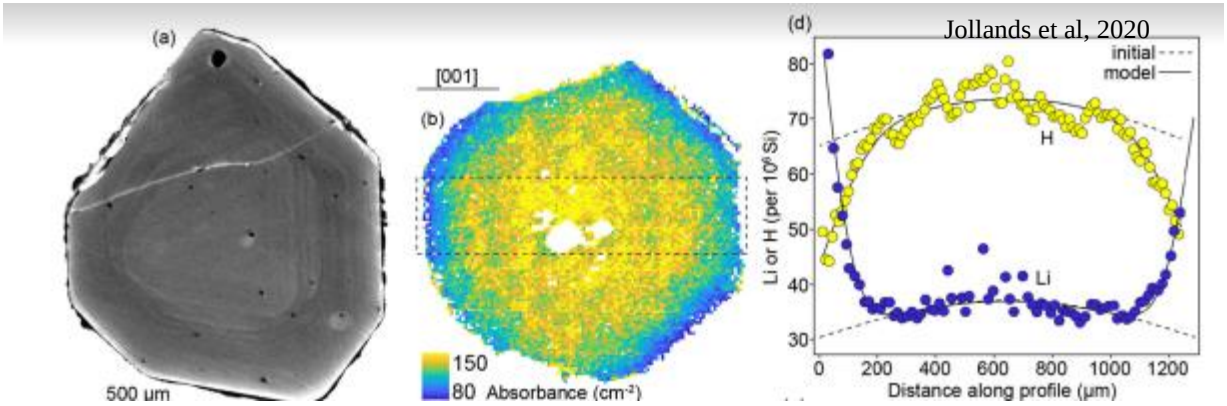

Fig.3 Concave-down water concentration gradient in a quartz phenocryst from the Bishop Tuff relating to the coupling of Li^+ with H^+.

Tollan et al. (2019) describe a technique for measuring the H^2O and CO_2 concentrations of melt inclusions fully enclosed in quartz crystals using transmission FTIR, where melt inclusion thickness is calculated using the host quartz silicate absorption overtones. Tollan et al. (2019) observed a sharp decline in OH^- in the outermost 200 um rims of the quartz analyzed and this anti-correlated with Li-O. The presence of Al^{3+} in their study was also observed in the acquired profiles by FTIR and LA-ICP-MS. A clear decrease in hydroxyl concentrations from core to rim

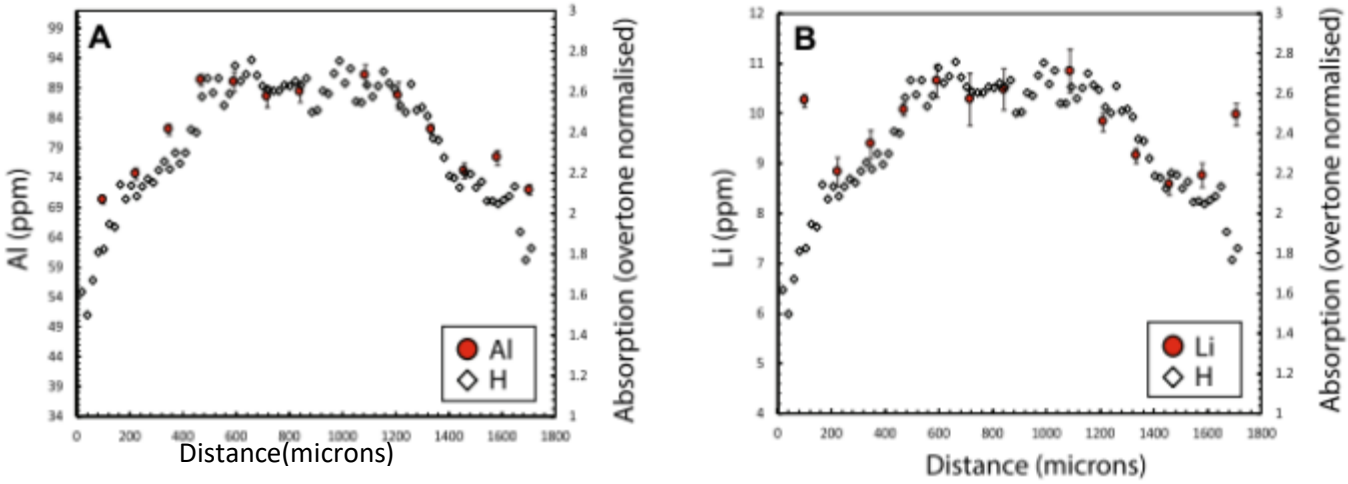

Fig.4 The presence of trace elements coupling with H^+ shows the same water concentration gradient observed by Jollands et al. (2020) with the Li^+ having a gradient variations and given that Al^{3+} diffuses slowly the figure reflects a solubility gradient rather than a diffusion gradient. Absorption(overtone normalized) in this case is equivalent to the integrated absorbance of elements present in the quartz phenocrysts.

matches closely the zoning in Al, which combined with the position of quartz infrared bands, most likely reflects variations in Al-moderated OH^- solubility rather than diffusive loss. This is illustrated in (**fig. 4**) seen above. The presence of trace elements coupling with H^+ shows the same water concentration gradient observed by Jollands et al. (2020) with the Li^+ having a gradient variation and given that Al^{3+} diffuses slowly the figure reflects a solubility gradient rather than a diffusion gradient. It can also be seen in **fig. 4b**, on the edges of the crystal on the right, the Li concentration goes up and the H concentration shows a downward slope. This indicates that there was some Li-H exchange at the edge, possibly during magma decompression.

4. Methods

The samples used for this study are from Cerro Machin volcano and were collected by Silvia Castilla. Two quartz crystals were picked from the crushed samples from one fall deposit layer which was split up into three different sections: the top, middle and bottom layers (**Fig. 5a**). These samples were crushed to get suitable sized quartz crystals for analysis (minimum size of 300 microns) and their original shape was observed to have the original edges after crushing the samples (hexagonal crystal habit observed). The crystals were picked from crushed samples from the middle layer deposition using a microscope. The individual quartz crystals were then mounted on glass polishing plates and held down using Crystal Bond for polishing. The selected crystals were oriented such that their crystallographic c axis lay horizontally on the glass slides. According to Hencz et al. (2021), to get the maximum absorbance, the crystal should be oriented along the c-axis and the incident infrared radiation should be polarized such that its vibration direction is parallel to the crystallographic c-axis. After mounting the crystals, the samples were polished to the proper thickness(0.0327cm and 0.0459cm) using various grades of aluminum oxide grinding paper (from 500 microns to 1 micron). The thickness is important as it is needed in calculating the water concentration present in each of the quartz phenocryst analyzed. After polishing one side of the crystal and taking pictures, the crystal bond was heated, and this

process released the crystal and made it easier to flip the crystal to the other side. Then the second side of the crystal was polished. Several crystals were doubly polished with the success of three out of 15 crystals coming out fine without breaking.

After polishing, the crystals were cleaned and inserted into the Nicolet iN10 MX Fourier Transform Infrared spectrometer (FTIR) to map the water gradients in the crystals. Following the settings used in Hencz et al. (2021), unpolarized light, an aperture of 50×50 μm with the collection time set to 25 seconds and 128 scans were used. The FTIR provides a spectrum for the different points selected and the spectra were analyzed using the OMNIC software.

During the measurements, a background was measured (image of what the background relatively looks like is shown in the Appendix) and subtracted from the data using the OMNIC software, and this was used to eliminate the contribution of water vapor and CO_2 from the atmosphere as the volatiles can affect the gradient mapped by changing the region at which the H_2O peaks appear. The spectra were obtained carefully from parts of the crystal where melt inclusions were not visible. Measurements along the crystal edge to core to edge were acquired both from N-S and E-W traverses of the crystals.

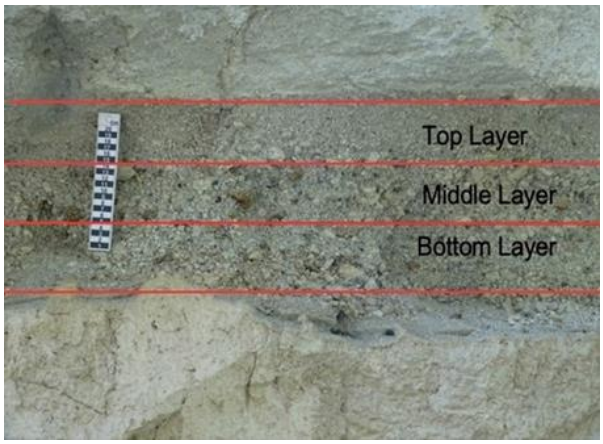

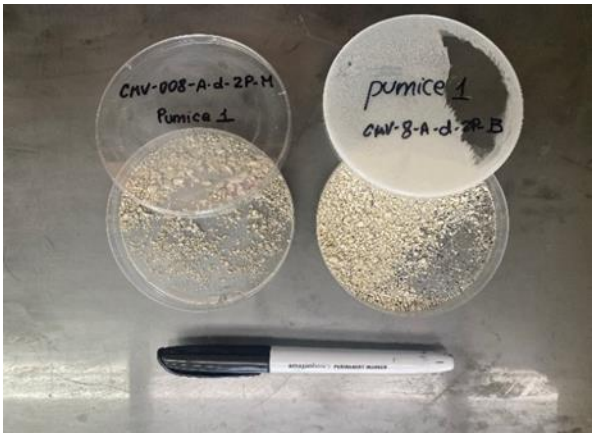

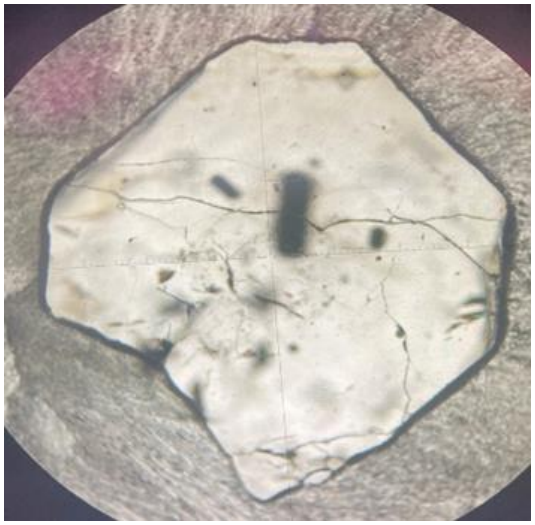

Fig. 5a. Layers from which the quartz crystals were picked. The red lines show the boundaries of the top, middle and bottom layers. Scale is in cm.
Fig. 5b. The crushed samples collected from the middle and bottom layers
Fig. 5c. The polished surface of one quartz crystal collected from the bottom layer.

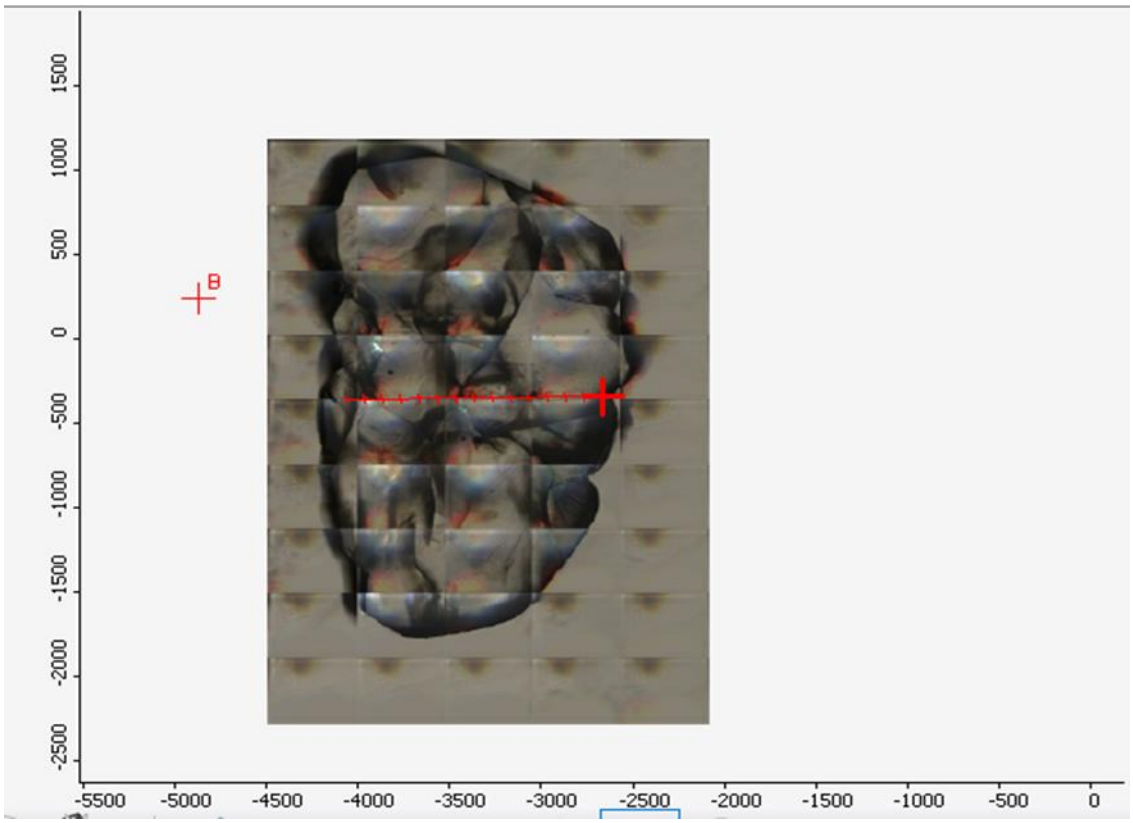

Fig.6 Mosaic of the quartz crystal from the lower layer of the deposition with points picked for measurements. The point B marks the background set to eliminate the atmospheric CO_2 and water vapor. The red line across the crystal shows the points chosen going from E-W. The points chosen on this crystal goes from 0 μm to 1300 μm (one edge to the other edge).

5. Results

As of last semester, my goal for this research was to calculate the water concentration of the quartz crystals using the modified Beer–Lambert law,

$$c = \frac{A_{tot} * M_i}{\varepsilon_i * \rho * t}$$

retrieved from Hencz et al. (2021) where A_{tot}= integrated absorbance (cm^{-1}); Mi = molar weight of water (18 g/mol); Ɛi= absorption coefficient (89000 ± 15000 L/mol cm^{-2} retrieved from Thomas et al., 2009); ρ= density of mineral (2650 g/L); t= thickness of sample (0.0327 and 0.0459 cm); and C= calculated water concentration (ppm). Note that the 'unmodified' Beer-Lambert law is.

$$A = \varepsilon * b * C$$

where A=absorbance; Ɛ= molar absorptivity; b=length of light path and C=concentration: however, given that the thickness and density of the crystal as well as the molar weight of water is needed to calculate the water concentration in quartz, the modified version of the equation is more suitable. Note also that the integrated absorbance is the sum of polarized light

measurements made in multiple orientations through the crystals, but we used unpolarized light for the measurements. According to Jollands et al. (2020), the integrated absorbance can be approximated as 4xAbs using unpolarized light assuming that the crystallographic c axis is in the crystal slab, so the unpolarized absorbance measurements were multiplied by a factor of 4.

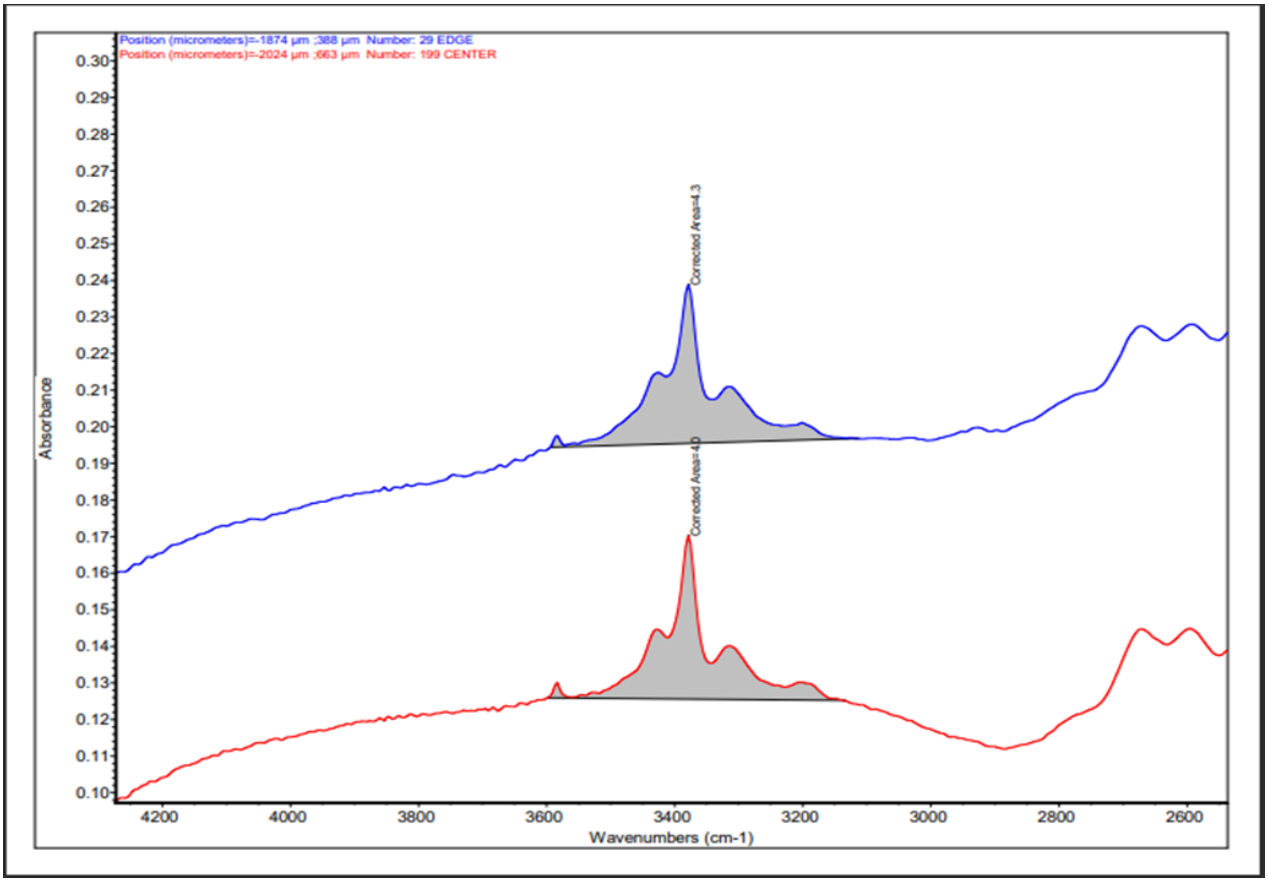

Fig.7 Area shaded under curve correlates with water concentration with the blue curve representing the edge (area under blue curve= 4.3) and red curve represents the center= 4.0.
The red and blue curves both have a starting absorbance point which is at 0.10 micrometers, and they are offset to see the difference between the area under the curves.
At about 2900cm^{-1} the small peak in the blue curve is due to the residue of the crystal bond (organics) still on the crystal. This feature is absent in the red spectrum, suggesting that the crystal bond was completely removed.

Some points measured in the quartz show some anomalies between 3700cm^{-1} and 3500cm^{-1} (**fig.8**); these anomalies appear as shoulders that have higher peaks than normal (a normal profile with no anomalies should look like the gradients shown in **fig.7**). These higher

peaks are indications of the influence of fluid or melt inclusions as the light beam travels through the fluid inclusion or crack.

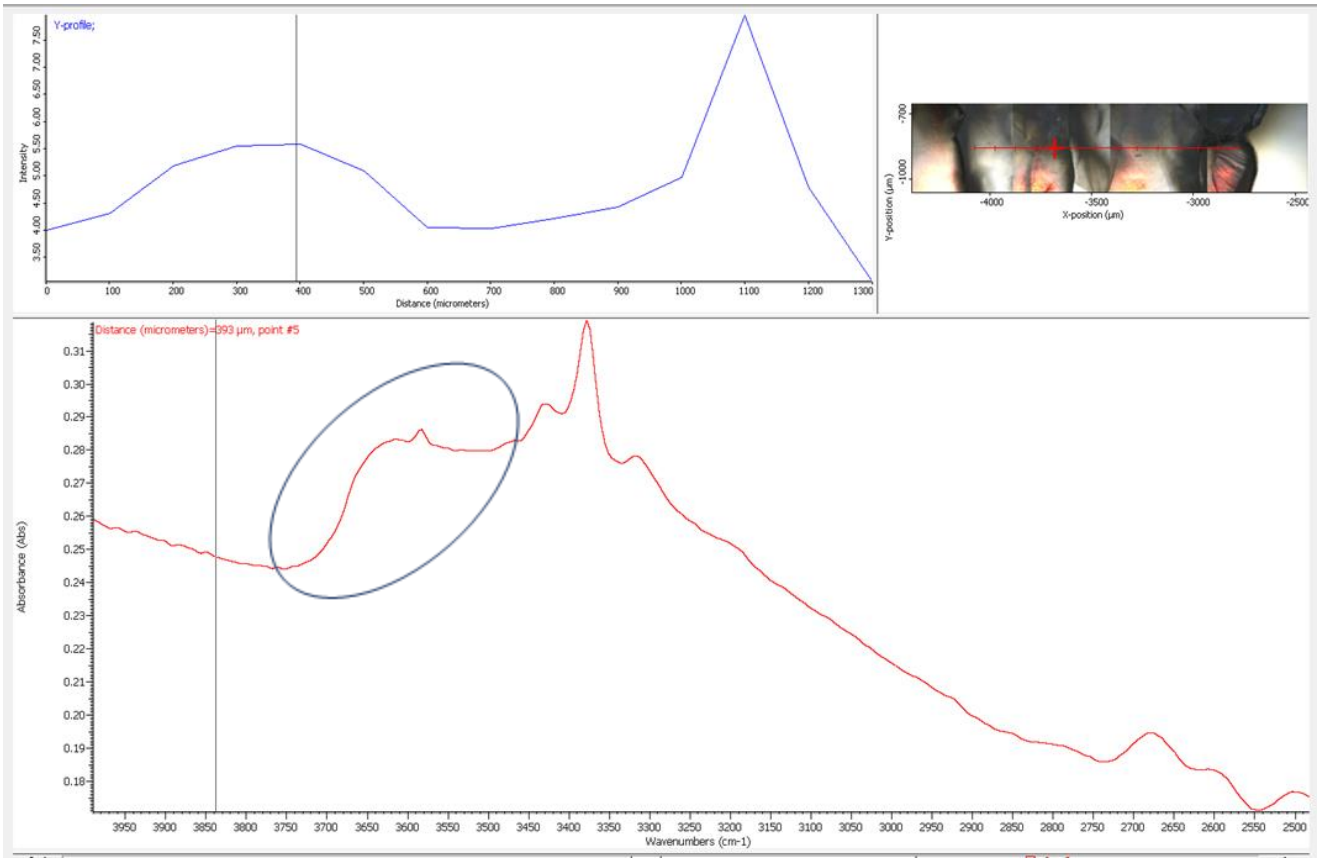

Fig. 8. Different points chosen on the crystal going from E-W as shown in the top right corner of the image above. The points range from 0 µm to 1300 µm. However, some of the points (as shown in the top left corner of the image) ranging from around 300 µm to 500 µm and 1100 µm to 1300 µm have shoulders when the absorbance is plotted against the wavenumbers at around wavenumber of 3600cm^{-1} (as shown in the lower section of the image) which would indicate melt or fluid in the path of the beam.

The points that show these anomalies include points; 300 µm, 400 µm, 500 µm, 1100 µm, 1200 µm, 1300 µm. The water concentrations in ppm were calculated using the modified Beer–Lambert law retrieved from Hencz et al. (2021) for all the points (0 µm to 1300 µm) measured on the crystal in the east to west direction and the results are shown in Table 1 below.

Measurements from East to West of crystal from bottom layer of deposition (Table 1)

microns	integrated absorbance	I.A*4	density	thickness	M.W water	epsilon	water concentration	water concentration
μm	cm^{-1}	cm^{-1}	g/L	cm	g/mol	$Lmol^{-1}cm^{-2}$	weight fraction	in ppm
0	4.00	16.02	2650	0.0326	18	89000	3.75E-05	37.5
100	4.32	17.27	2650	0.0326	18	89000	4.04E-05	40.4
200	5.18	20.73	2650	0.0326	18	89000	4.85E-05	48.5
300	5.55	22.20	2650	0.0326	18	89000	5.20E-05	52.0
400	5.58	22.33	2650	0.0326	18	89000	5.23E-05	52.3
500	5.08	20.33	2650	0.0326	18	89000	4.76E-05	47.6
600	4.06	16.23	2650	0.0326	18	89000	3.80E-05	38.0
700	4.04	16.16	2650	0.0326	18	89000	3.78E-05	37.8
800	4.22	16.87	2650	0.0326	18	89000	3.95E-05	39.5
900	4.42	17.70	2650	0.0326	18	89000	4.14E-05	41.4
1000	4.97	19.89	2650	0.0326	18	89000	4.66E-05	46.6
1100	7.97	31.87	2650	0.0326	18	89000	7.46E-05	74.6
1200	4.80	19.19	2650	0.0326	18	89000	4.49E-05	44.9
1300	3.07	12.27	2650	0.0326	18	89000	2.87E-05	28.7

The calculated water concentrations (with a range of 28-74 ppm) are plotted as a function of distance across the crystal in **fig. 9**. In Fig. 9a, we plot all points, including those with spectra that show contamination with melt/fluid (at 300 μm, 400 μm, 500 μm, 100 μm, 1200 μm, 1300 μm). The water concentration does not follow a clear diffusion pattern (fig. 9a.). When the melt-contaminated points are removed as shown in **fig. 9b**, there is still no clear evidence that water is diffusing out of the crystal. The water concentrations decrease towards the edge of the crystal (between 0 and 200 μm), but the magnitude of the water concentration decrease is small and may be a result of random error.

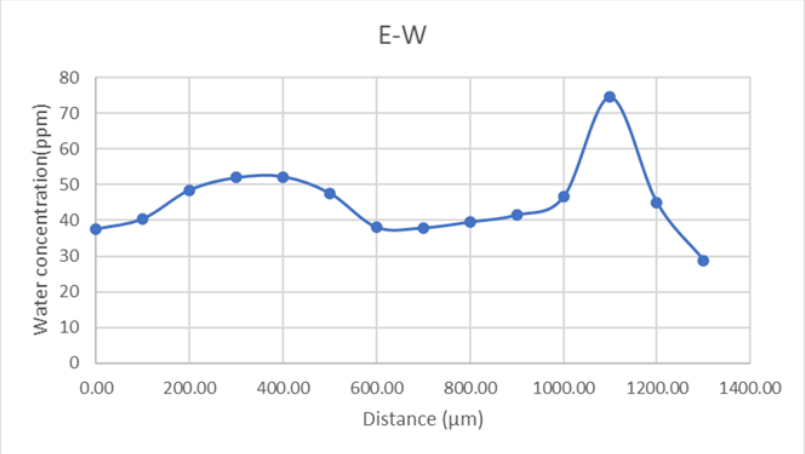

Fig. 9a. Plot of the water concentration (ppm) against all the points chosen (μm) including the points with the anomalies on the crystal in the E-W direction

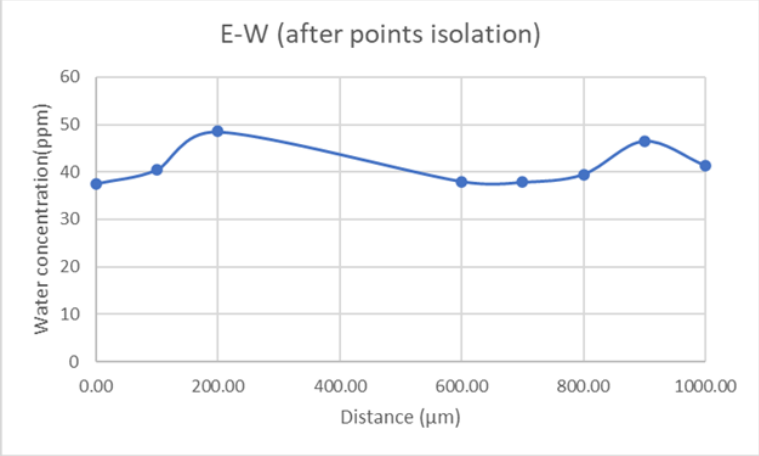

Fig. 9b. Plot of the water concentration(ppm) against the points without contaminations (µm) in the E-W direction

In addition to the E-W traverse shown in **fig. 9**, I also measured a perpendicular traverse along the N-S direction of the crystal. From the points chosen along the north to south path, there were some points that showed the same type of melt contamination found in the mapping of the crystal in the east to west direction and these points are at 200 µm, 300 µm, 600 µm, 700 µm, 800 µm, 900 µm, 1000 µm, 2100 µm. The water concentrations in ppm were also calculated using the modified beer lambert equation for all the points (0 µm to 2100 µm) measured on the crystal in the north to south direction and the results are shown in Table 2 below.

Measurements from North to South of the crystal (Table 2)

microns	integrated absorbance	I.A*4	density	thickness	M.W water	epsilon	water concentration	water concentration
µm	cm^{-1}	cm^{-1}	g/L	cm	g/mol	$Lmol^{-1}cm^{-2}$	weight fraction	ppm
0	5.10	20.40	2650	0.0326	18	89000	4.78E-05	47.8
100	5.66	22.62	2650	0.0326	18	89000	5.30E-05	53.0
200	6.77	27.10	2650	0.0326	18	89000	6.34E-05	63.4
300	6.05	24.21	2650	0.0326	18	89000	5.67E-05	56.7
400	5.47	21.86	2650	0.0326	18	89000	5.12E-05	51.2
500	5.52	22.10	2650	0.0326	18	89000	5.17E-05	51.7
600	6.22	24.89	2650	0.0326	18	89000	5.83E-05	58.3
700	4.30	17.20	2650	0.0326	18	89000	4.03E-05	40.3
800	5.06	20.25	2650	0.0326	18	89000	4.74E-05	47.4
900	4.86	19.43	2650	0.0326	18	89000	4.55E-05	45.5
1000	6.58	26.33	2650	0.0326	18	89000	6.16E-05	61.6
1100	5.14	20.57	2650	0.0326	18	89000	4.81E-05	48.2
1200	3.38	13.51	2650	0.0326	18	89000	3.16E-05	31.6
1300	3.42	13.67	2650	0.0326	18	89000	3.20E-05	32.0
1400	3.56	14.24	2650	0.0326	18	89000	3.33E-05	33.3
1500	4.76	19.03	2650	0.0326	18	89000	4.46E-05	44.6
1600	3.39	13.58	2650	0.0326	18	89000	3.18E-05	31.8
1700	6.22	24.88	2650	0.0326	18	89000	5.82E-05	58.3
1800	6.23	24.91	2650	0.0326	18	89000	5.83E-05	58.3
1900	6.70	26.79	2650	0.0326	18	89000	6.27E-05	62.7
2000	5.02	20.08	2650	0.0326	18	89000	4.70E-05	47.0
2100	4.29	17.15	2650	0.0326	18	89000	4.02E-05	40.2

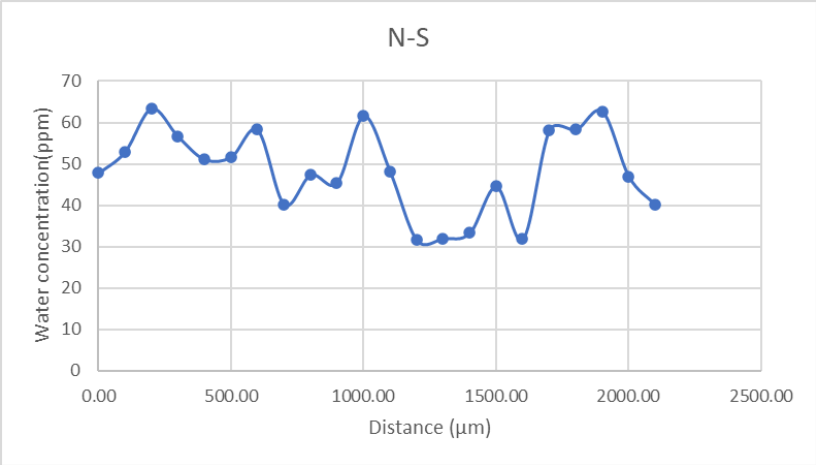

Fig. 10a. Plot of the water concentration (ppm) against all the points chosen (µm) including the points with the anomalies on the crystal in the N-S direction.

Fig. 10b Plot of the water concentration(ppm) against the points without contaminations (µm) in the N-S direction

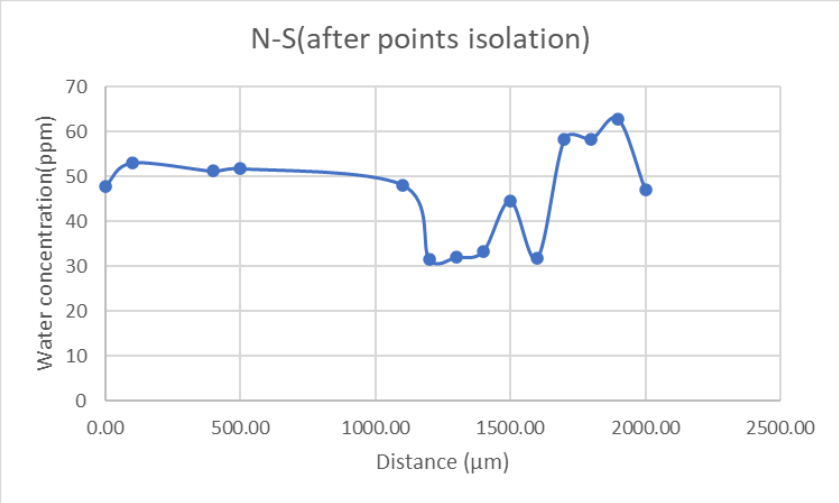

The next steps taken after creating these plots was comparing the N-S gradient to the gradient in the E-W direction and the pattern is the same shown when those points were isolated as shown in fig. 9b, at first the change was thought to be water being diffused out of the crystal, the water concentration are slightly decreasing in slope at the edges, however, the decrease at the edges is small compared to the overall scatter. The calculated water concentration of points chosen along the N-S path is ~48 ppm (with range 31-60 ppm). Interestingly, both profiles have the lowest water concentrations in the centers of the crystal (i.e., the overall profile is shaped like a letter 'M'). These results were from measuring points across the quartz phenocryst from one edge to another along a straight line.

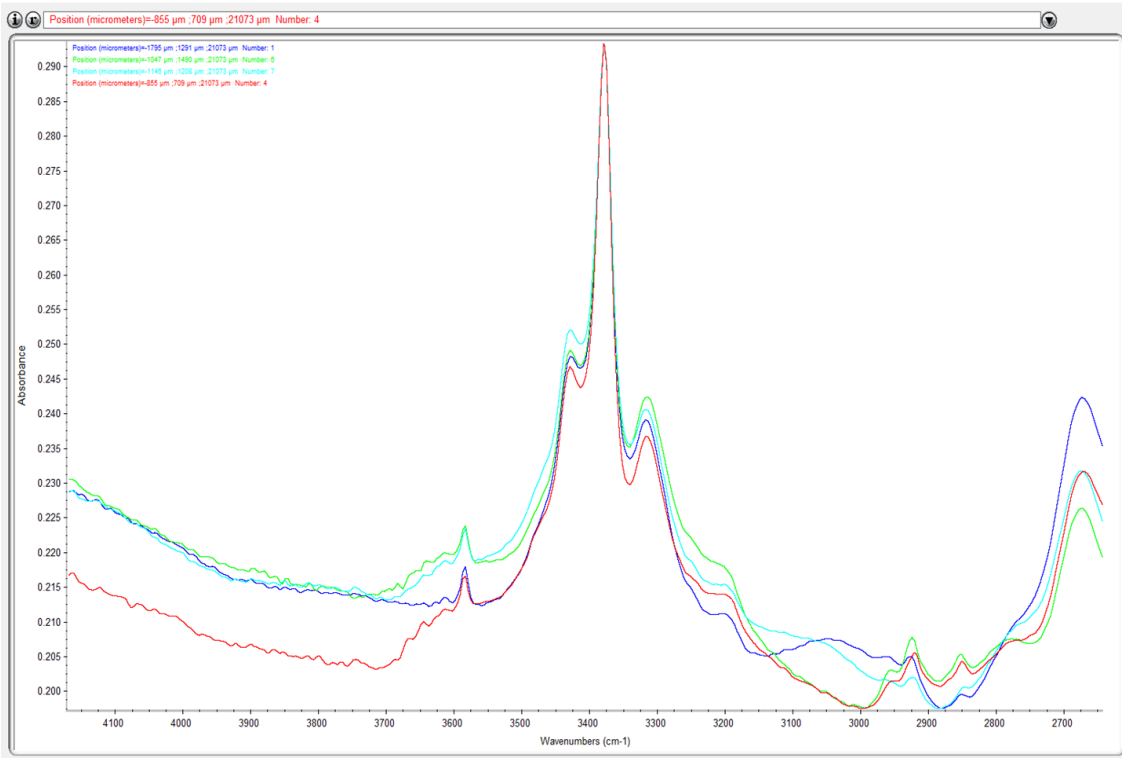

Fig. 11 Clean spectra without melt contamination produced by measuring the absorbance at individual points (making sure to avoid melt inclusions) at the center and the edges of the phenocryst.

However, given that a clean spectrum was not being produced from this method of measurement, another method was applied, and this involved measuring different points at the edges of the phenocrysts and a few spots at the center in order to produce cleaner spectra with no melt contamination (**Fig. 11**).

As stated previously, a different method was applied to pick points to be measured in order to get a clean spectrum and this was done by selecting a few points all around the edges and a few points at the center, the spectra produced was used to collect the integrated absorbance data and this was used to calculate the water concentration in two different quartz phenocrysts from the same deposition layer with different thickness. The error in the measured thickness is estimated to be approximately 1% based on three replicate measurements of samples 327 and 460 microns thick. The mean and standard deviation of the calculated water concentrations were derived, and the error bars were plotted for both the center and the edge water concentration for both of the phenocrysts. The results show that the water concentration at the edges and centers of both phenocrysts are uniform within the error (**fig 12**). Thus, the result of the newly applied method supports the uniform gradient of water observed in the East-West measurements (**fig.14**).

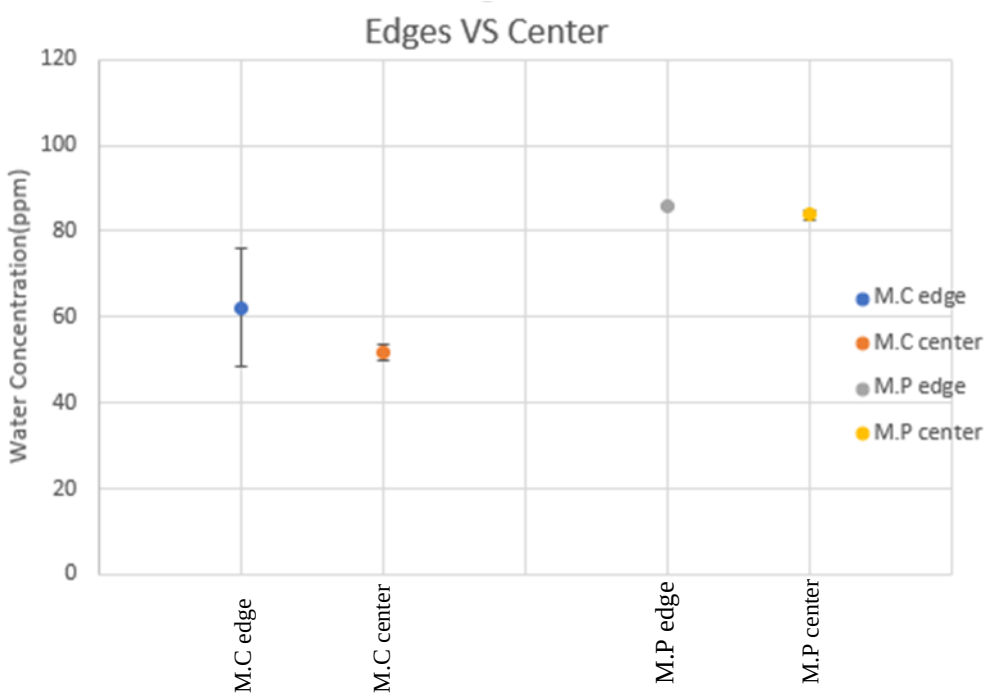

Fig. 12. Plot of the calculated water concentration of M.C and M.P phenocrysts at the edge and the center with error bars showing the uniform water concentration with error. Measurements documented in Table 3 below.

Table 3. Calculated water concentration of individual points at the edge and center of two quartz phenocrysts(M.C and M.P)

M.C quartz Microns Edge	Integrated Absorbance(cm^{-1})	I.A*4	Density g/L	Thickness cm	M.W water g/mol	Epsilon $Lmol^{-1}cm^{-2}$	Water conc. Weight Fraction	Water conc. (ppm)
1.00	7.50	30	2650	0.0459	18	89000	4.9E-05	49.9
3.00	12.22	48.88	2650	0.0459	18	89000	8.1E-05	81.3
4.00	8.33	33.32	2650	0.0459	18	89000	5.5E-05	55.4
Center								
6.00	7.88	31.52	2650	0.0459	18	89000	5.2E-05	52.4
7.00	8.08	32.32	2650	0.0459	18	89000	5.4E-05	53.7
8.00	7.42	29.68	2650	0.0459	18	89000	4.9E-05	49.4
M.P quartz Edge								
7.00	9.17	36.68	2650	0.0327	18	89000	8.6E-05	85.6
8.00	9.25	37.00	2650	0.0327	18	89000	8.6E-05	86.4
14.00	9.15	36.60	2650	0.0327	18	89000	8.5E-05	85.4
Center								
10.00	9.15	36.60	2650	0.0327	18	89000	8.5E-05	85.4
11.00	8.80	35.20	2650	0.0327	18	89000	8.2E-05	82.2
12.00	8.96	35.84	2650	0.0327	18	89000	8.4E-05	83.7

6. Discussion

Jollands et al. (2020) and Tollan et al. (2019) mentioned the effect that trace elements would have on water concentration gradients in quartz phenocrysts. This brings me to stating the types of gradients that would be expected if the quartz phenocrysts retrieved from Cerro Machin Volcano contains trace elements or not. A schematic of the concentration gradients against an average value of points at the center and

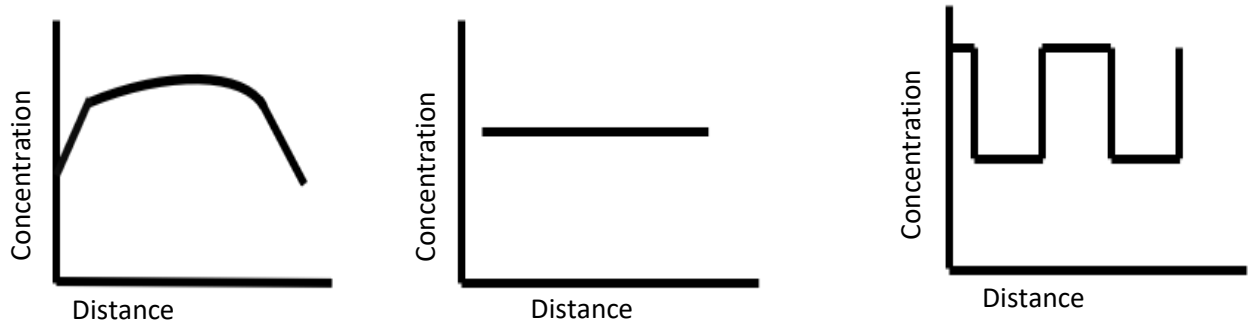

Fig.13a This schematic indicates a degassing gradient during eruption where water concentration is lower at edges and higher at the center
Fig.13b Very slow diffusion is indicated in this schematic and this could be due to the attachment and/or substitution of trace elements like Al^{3+}, such as $Si^{4+} = Al^{3+} + H^{+}$
Fig.13c this schematic illustrates a complex gradient that could indicate coupling of H^{+} with trace elements such as Li, B, Ti, Al etc.

edges of the phenocrysts are shown above (**fig.13**).

Although water concentration gradients were not observed in the analyzed quartz phenocrysts and although concentration gradients in quartz phenocrysts were not observed, the absence of gradients can be used to constrain an upper bound on the duration of magma ascent. The diffusion coefficient (i.e., speed of water diffusion) represented as D from Jollands et al. (2020) was calculated by using the equation

$$log_{10}\mathrm{D} = log_{10}D_0 + \frac{-E_a}{2.303\mathrm{RT}}$$

where $\log_{10}D_0$ is $\log_{10}D$ at $1/T=0$ ($m^2\ s^{-1}$), E_a is the activation energy for diffusion (kJ mol^{-1}), R is the gas constant (kJ K^{-1} mol^{-1}), and T is in Kelvin According to Jollands et al. (2020) the Ea=100.4 ± 5.2 kJ mol^{-1} and at a temperature of 855 ºC, the logD is -11.14. An analytical solution was applied to the 1D diffusion equation for all points derived after the contamination isolation from the east to west measurements (blue circles in fig. 13 below) to calculate the duration of magma ascent which is 1.25 minutes. The standard deviation for the points without the anomalies (**fig.9b**) were calculated to be 3.9 and the points as shown in the figure below appear to have a uniform water concentration within the same error. Although, from the work done last semester and the downward water concentration seen in the phenocryst appears to be scattered variation occurring along the measured points. Given that the size of the beam spot of the FTIR was measuring over an average of 50 um^2 area, gradients that were within this area could not be resolved and concentration measurements could not be detected because the spot size is big.

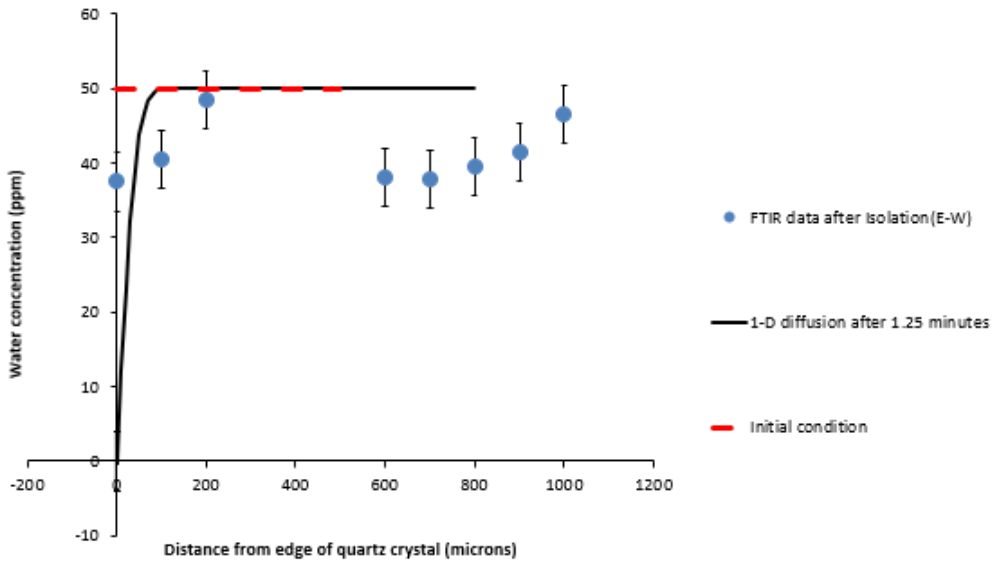

Fig.14 Plot produced using the 1D-diffusion equation from Jollands et al. (2022) to calculate the duration of the magma ascent rate. The initial water concentration condition is also shown as well as the relatively uniform gradient within error of the East-West measurements after the isolation.

To check the gradients that are within the 50 um^2 area, the time in the model was adjusted until the distance was at approximately 50-micron from the edge at 1.25 minutes and although the plot shows a downward curve, an accurate gradient curve cannot be given because the beam size gave an average of the variations occurring at the edge, not individual variations. **Table 4** contains measurements used to plot the water concentrations over the 50-micron averaged edge area.

Table 4: Calculated concentration measurements using the duration of magma ascent

Distance(microns)	Distance(m)	Calculated concentrations(wt%)
0	0	0
10	1.0E-05	1.2E+01
20	2.0E-05	2.3E+01
30	3.0E-05	3.2E+01
40	4.0E-05	3.9E+01
50	5.0E-05	4.4E+01
60	6.0E-05	4.7E+01
70	7.0E-05	4.8E+01
80	8.0E-05	4.9E+01
90	9.0E-05	5.0E+01
100	1.0E-04	5.0E+01
110	1.1E-04	5.0E+01
120	1.2E-04	5.0E+01
130	1.3E-04	5.0E+01
140	1.4E-04	5.0E+01
150	1.5E-04	5.0E+01

160	1.6E-04	5.0E+01
170	1.7E-04	5.0E+01
180	1.8E-04	5.0E+01
190	1.9E-04	5.0E+01
200	2.0E-04	5.0E+01
210	2.1E-04	5.0E+01
220	2.2E-04	5.0E+01
230	2.3E-04	5.0E+01
300	3.0E-04	5.0E+01
400	4.0E-04	5.0E+01
500	5.0E-04	5.0E+01
600	6.0E-04	5.0E+01
700	7.0E-04	5.0E+01
800	8.0E-04	5.0E+01

According to Jollands et al. (2020) and Tollan et al. (2019), the presence of trace element substituting with Si^{4+} and coupling with H^{+} can affect the water diffusion gradient in quartz and in this case the presence of an aluminum peak was observed in the spectra as this peak was compared to have the same wavenumber limits as stated in Jollands et al. (2020). The Al^{3+} peak was stated to be at 3377cm^{-1} and the peak observed in my spectra was at 3375cm^{-1}, however, a Li-O peak was not observed at the expected wavenumber of 3482cm^{-1}. Given the presence of Al^{3+} and its slow diffusion, there is a possibility that Al either substituted for Si in the case or it is coupling with H and the diffusion did not have enough time to occur due to the fast magma ascent rate. It was also reported by Tollan et al. (2019) that the gradient that was observed was influenced by Al and their observation could be the solubility curve of H^{+} rather than a diffusion gradient; this is another possibility of what is observed in my research. However, for this research, it is being assumed that the Jollands diffusion coefficient applies even though the diffusion coefficient is specifically for lithium-hydrogen exchange and a lithium peak was not observed in this case, therefore it is hard to say if the diffusion coefficient used would be sufficient for this problem given that we do not have a diffusion coefficient that applies to a proton-Aluminum exchange.

The magma storage of Cerro Machin volcano has a minimum pressure of 100MPa and a maximum pressure of 500MPa as determined by Silvia Castilla and given that the magma ascent rate time is about 1.25 minutes (75 s), this can be used to find the decompression rate given as,

$$\frac{pressure}{time}$$

and this gives a decompression rate for the minimum and maximum pressure as 1.33 Mpa/s and 6.67 Mpa/s. As shown in table 4 below, the magma depth was calculated to be 3580 m and 17901 m for both pressures using the equation

$$h = \frac{P}{\rho * g},$$

where P = pressure; ρ = lithostatic gradient (the density of the crust) and according to Ferguson et al. (2016) the depth is estimated assuming a lithostatic gradient with a crustal density of

2850kg/m^3. The speed at which the magma was travelling was also calculated for both the minimum and maximum pressure and estimated to be about 47.7 m/s for the minimum pressure and 238.7 m/s for the maximum pressure.

	Pressure	Pressure	Decompression Rate	Acceleration of Gravity	Magma Depth	Magma Speed
	MPa	N/m^2	(MPa/s)	(m/s^2)	(m)	(m/s)
Minimum	100	100000000	1.3	9.8	3580.4	47.7
Maximum	500	500000000	6.7	9.8	17901.9	238.7

Table 5. For the calculation of the magma depth and speed, the ascent time was converted to be 75 seconds from 1.25 minutes, and the lithostatic gradient (crustal density) was assumed to be 2850 kg/m^3).

Comparing the decompression rates calculated in this study to other works done on decompression rate of other volcanoes, the rates seem to fall within the expected range as shown in the **Fig. 15.** below. The plot below displays ascent and decompression rate data from a range

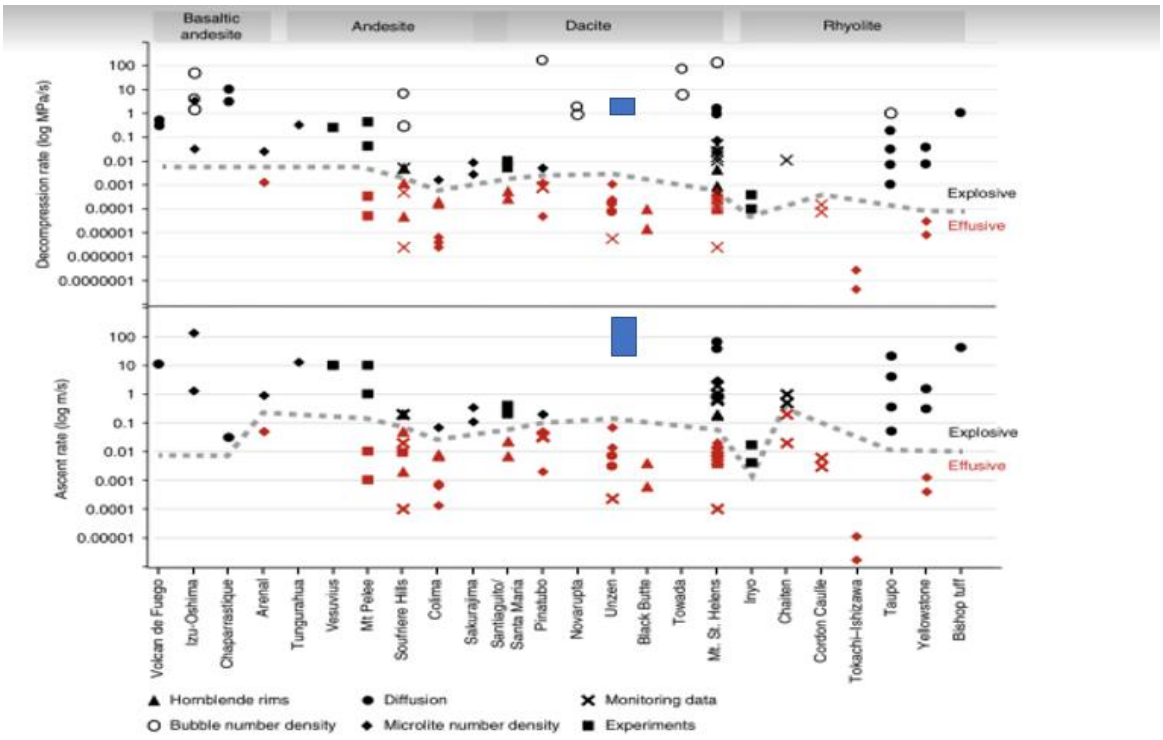

Fig.15. Comparison of different ascent rates and decompression rates estimates from multiple volcanoes ranging from basaltic andesite to rhyolites. This plot ascent and decompression rate data from a range of different techniques, including bubble number density, experiments, hornblende rims, extrusion rate and diffusion rates. The decompression rate calculated in this study falls between ~1.33MPa/s and ~6.67MPa/s as indicated with the purple box. From Cassidy et al.(2018).

of different techniques, including bubble number density, experiments, hornblende rims, extrusion rate and diffusion rates from multiple volcanoes. The decompression rate for diffusion calculated in this study falls between ~1.33 MPa/s and ~6.67 MPa/s as indicated with the blue boxes with the magma speed between ~48 to ~239 m/s and seems to be in range when compared

to the basaltic and dacite decompression rates. This range also falls above the effusive-explosive line which supports the explosive eruption style of Cerro Machin Volcano.

7. Conclusions

The amount of water in magma controls the viscosity of the magma as well as the depth at which vapor bubbles are formed. Another important factor is the magma decompression rate which controls the time available to form bubbles and crystals as well as the time available for vapor to escape the system. For this study, water concentration gradients were measured in quartz crystals from the eruption that occurred 3600 yr. BP (before present) which is known to be the biggest eruption to have occurred in the history of Cerro Machin volcano. Quartz crystals were used in this study instead of olivine due to the lack of olivine crystals in dacitic volcanoes such as Cerro Machin volcano. After measuring the water gradient in the quartz crystals using FTIR, the area under the curve which correlates to the absorbance was used to calculate the water concentration(ppm) using the modified Beer Lambert rule retrieved from Hencz et al. (2021) and this was also used for diffusion modelling to constrain the magma decompression rate as well as the duration of the magma ascent. The calculations done in this study suggests that the magma originated from a depth of ~17 km (table 5)with an ascent time of ~1.25 minutes and the magma storage as minimum pressure of ~100 Mpa and a maximum pressure of ~500 Mpa. The calculated mean water concentrations of the individual points selected at the edge and center of M.C quartz are ~62.2ppm and 51.83ppm, respectively, while the calculated mean water concentrations of the individual points selected at the edge and center of M.P quartz are ~85.79ppm and 83.74ppm, respectively, given that they differ in thickness. Comparison to other works done of decompression rate of diffusion suggests that the decompression rates calculated in this study falls within the expected ranges and it also falls above the effusive-explosive line which supports the explosive eruption style of Cerro Machin volcano.

Appendix

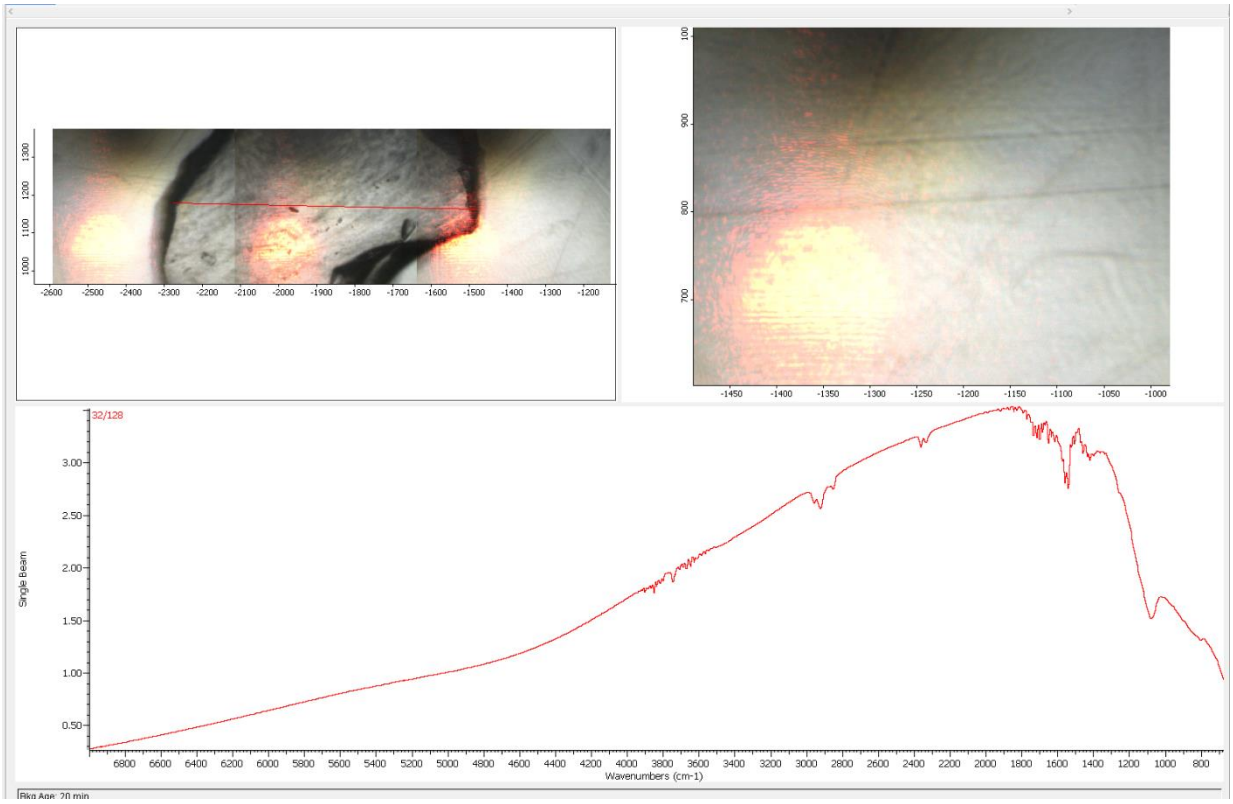

Fig.16. Illustration of what the collected backgrounds look like before the data absorbance spectrum is collected. For each of the quartz phenocrysts analyzed had relatively the same background.

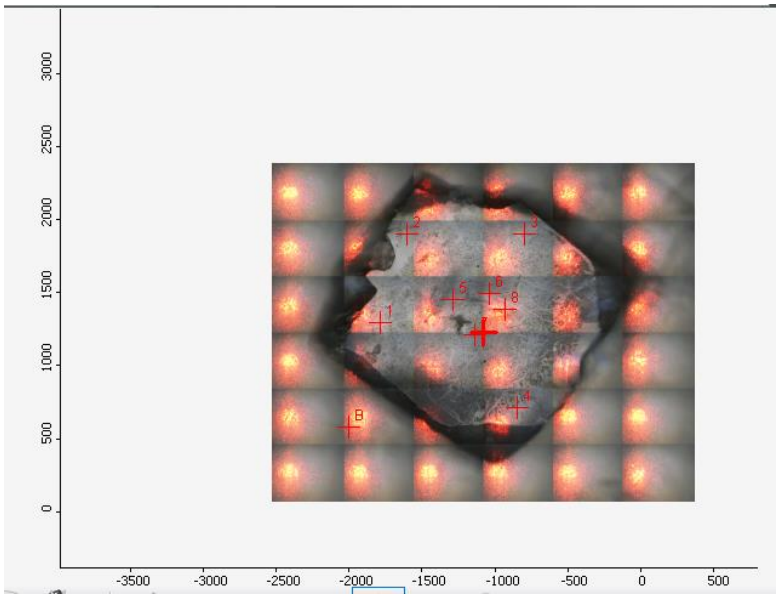

Fig. 17. Image showing the different method that was applied to pick points to be measured in order to get a clean spectrum. This was done by selecting a few points all around the edges and a few points at the center

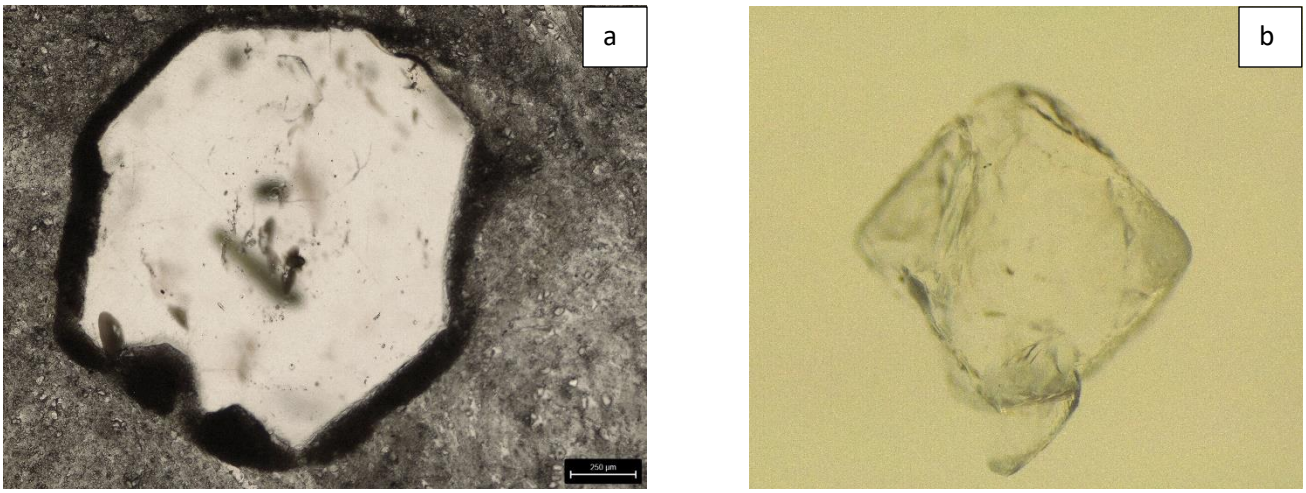

Fig.18a M.C quartz in crystal bond during polishing and this was picked form the middle layer of deposition
Fig.18b M.C quartz before polishing and this image illustrates the phenocryst retaining its original shape after the rock sample was crushed.

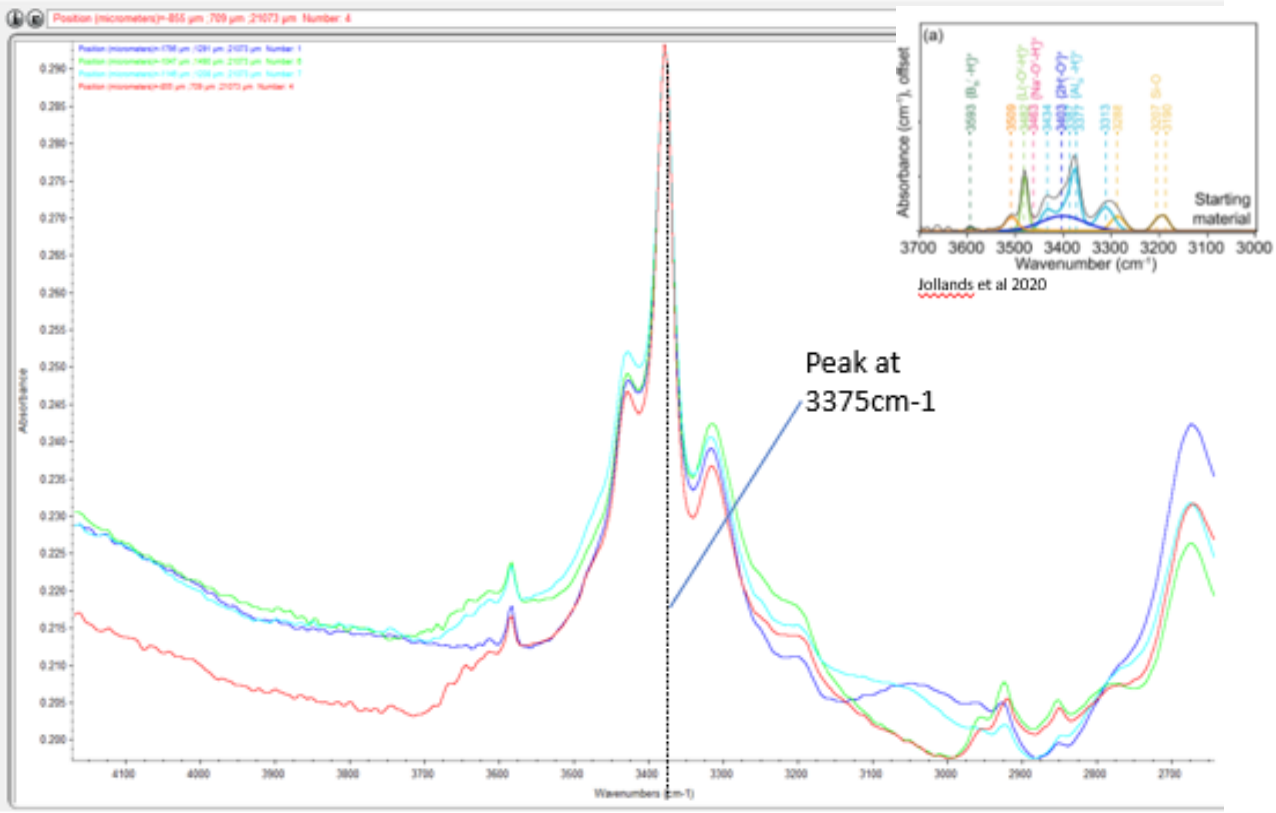

Fig.19. Comparing my peak results to the wavenumbers of different trace elements provided in the Jollands et al. (2020). This provides evidence of Al^{3+} in my analyzed quartz phenocrysts
No Li-O peak observed

References

British Geological Survey (2021). Eruption Styles. https://www.bgs.ac.uk/discovering-geology/earth-hazards/volcanoes/eruption-styles/

Cassidy, M., Manga, M., Cashman, K., and Bachmann, O. (2018). Controls on explosive effusive volcanic eruption styles. *Nature Communications*, *9*(1), 1–7. https://doi.org/10.1038/s41467-018-05293-3

Ferguson, D. J., Gonnermann, H. M., Ruprecht, P., Plank, T., Hauri, E. H., Houghton, B. F., & Swanson, D. A. (2016). Magma decompression rates during explosive eruptions of Kīlauea volcano, Hawaii, recorded by melt embayments. *Bulletin of Volcanology*, *78*(10), 1-12. https://link.springer.com/article/10.1007/s00445-016-1064-x

Global Volcanism Program (2012). Report on Machin (Colombia) (Herrick, J.A., and Wunderman, R., eds.). Bulletin of the Global Volcanism Network, 37:11. Smithsonian Institution. https://doi.org/10.5479/si.GVP.BGVN201211-351040

Hencz, M., Biró, T., Kovács, I. J., Stalder, R., Németh, K., Szakács, A., Pálos, Z., Pécskay, Z., & Karátson, D. (2021). Uniform "water" content in quartz phenocrysts from silicic pyroclastic fallout deposits – implications on pre-eruptive conditions. *European Journal of Mineralogy*, *33*(5), 571–589. https://doi.org/10.5194/ejm-33-571-2021

Jollands, M. C., Ellis, B., Tollan, P. M., & Müntener, O. (2020). An eruption chronometer based on experimentally determined H-Li and H-Na diffusion in quartz applied to the Bishop Tuff. *Earth and Planetary Science Letters*, *551*, 116560. https://www.sciencedirect.com/science/article/pii/S0012821X20305045

Rueda, H., Macias, J., Siebe, C., Cepeda, H., Mendez, R., & Cortes, G. (2005). Holocene Eruptions of Machin Volcano: Stratigraphy and Eruptive Dynamics. In *AGU Fall Meeting Abstracts* (Vol. 2005, pp. V53B-1551). https://ui.adsabs.harvard.edu/abs/2005AGUFM.V53B1551R/abstract

Thomas, Sylvia-Monique, et al. "IR Calibrations for Water Determination in Olivine, R-geo$_2$, and SIO_2 Polymorphs - Physics and Chemistry of Minerals." *SpringerLink*, Springer-Verlag, 5 Mar. 2009, https://link.springer.com/article/10.1007/s00269-009-0295-1

Tollan, P., Ellis, B., Troch, J.(2019). Assessing magmatic volatile equilibria through FTIR spectroscopy of unexposed melt inclusions and their host quartz: a new technique and application to the Mesa Falls Tuff, Yellowstone. *Contrib Mineral Petrol* **174**, 24 https://doi.org/10.1007/s00410-019-1561-y